Prussian Blue Analogues for Potassium-ion Batteries: Insights into the Electrochemical Mechanisms

Phuong Nam Le Pham[ab], Romain Wernert[acd], Maëlle Cahu[a], Giuliana Aquilanti[e], Moulay Tahar Sougrati[abd], Patrik Johansson[bf], Laure Monconduit[abd], and Lorenzo Stievano*[abd]

a)   ICGM, Univ. Montpellier, CNRS, Montpellier, France
b)   Alistore-ERI, CNRS, Amiens, France
c)   Univ. Bordeaux, CNRS, Bordeaux INP, ICMCB, UMR 5026, Pessac, France
d)   RS2E, CNRS, Amiens, France
e)   Elettra-Sincrotrone Trieste, Trieste, Italy
f)   Department of Physics, Chalmers University of Technology, Göteborg, Sweden
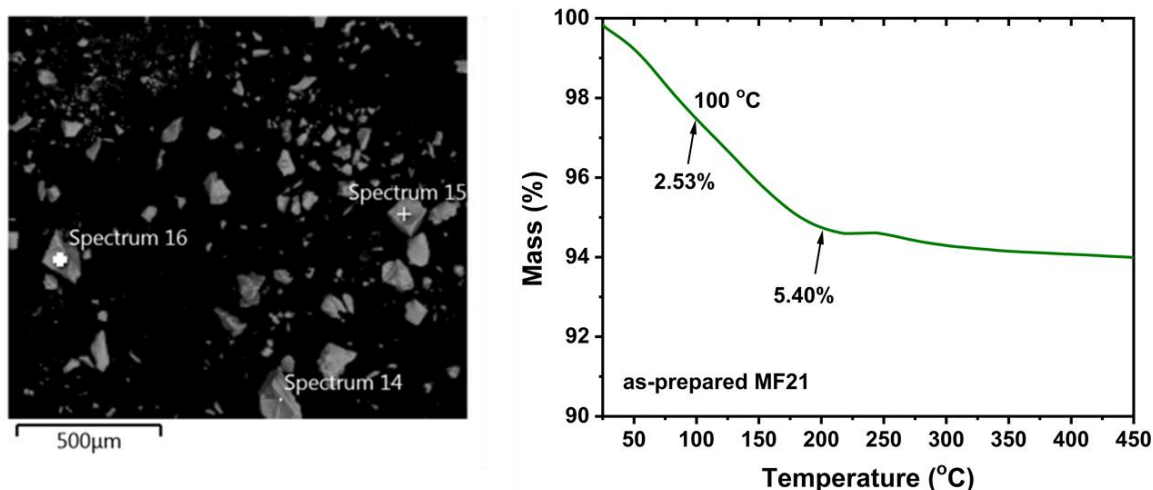
Supporting information

Figure S1. SEM-EDX image (left) and TGA curve (right) of the as-prepared MF21. The amount of removed water from the vacuum drying step is calculated from the mass loss at 100 ℃.

As observed in the TGA curve of MF21 (Figure S1), when increasing the temperature, the mass of MF21 keeps being lost until 200 ℃. However, it was reported that drying PBA at 200 ℃ for a long duration can cause structural damage.[1] In order to choose an appropriate drying temperature, we compared the color and the crystallinity of MF21 after the vacuum drying at 100 ℃ and 200 ℃ (Figure S2). When drying at 100 ℃, MF21 maintained its deep green color and monoclinic structure. In contrast, after one night being dried at 200 ℃, the material turned black and the main peaks corresponding to the monoclinic phase diminished, indicating a severe loss in the crystallinity. Therefore, we decided to dry MF21 at 100 ℃, which is enough to remove the interstitial water as well as to retain the material structure.
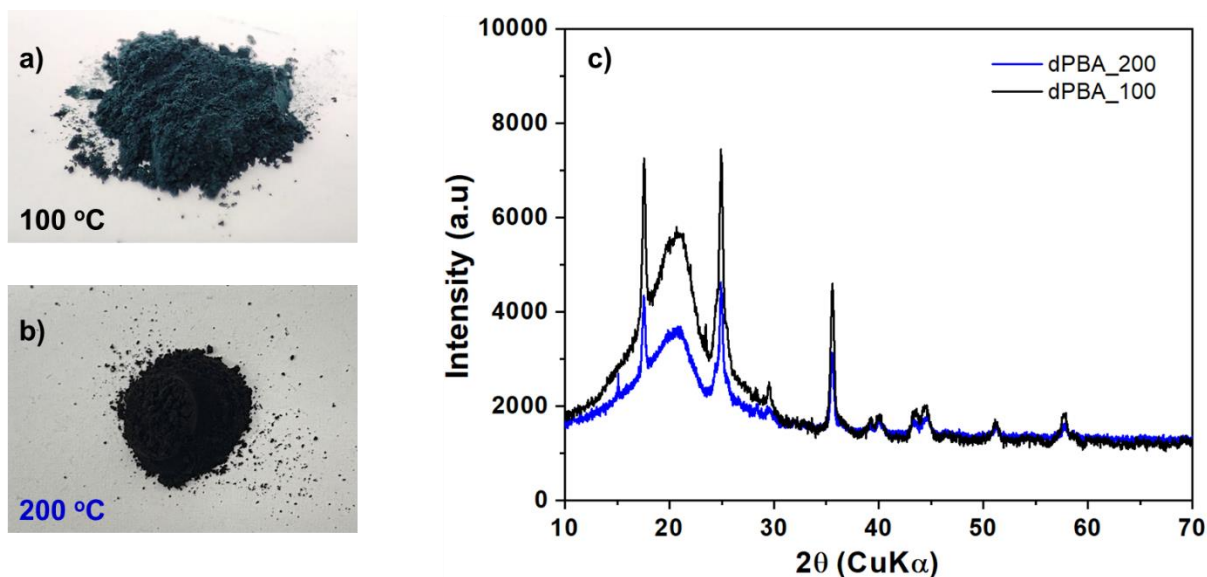
Figure S2. PBA powders after the vacuum drying at 100 °C (a) and 200 °C (b) and their X-ray diffractograms (c).

Table S1. Elemental analysis of K, Mn, and Fe obtained from SEM-EDX.

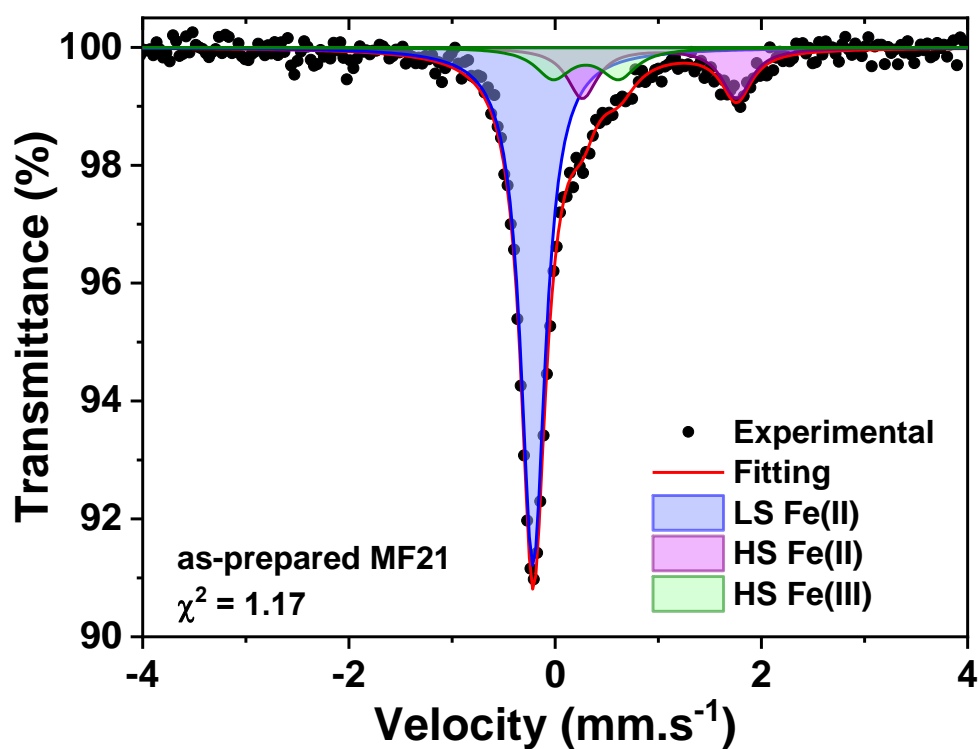| Element	K	Mn	Fe
Atomic percentage (%)	46.6	18.2	35.2

Figure S3. Room-temperature Mössbauer spectrum of pristine MF21.

Table S2. Refined Room-Temperature ^{57}Fe Mössbauer Hyperfine Parameters for pristine MF21.

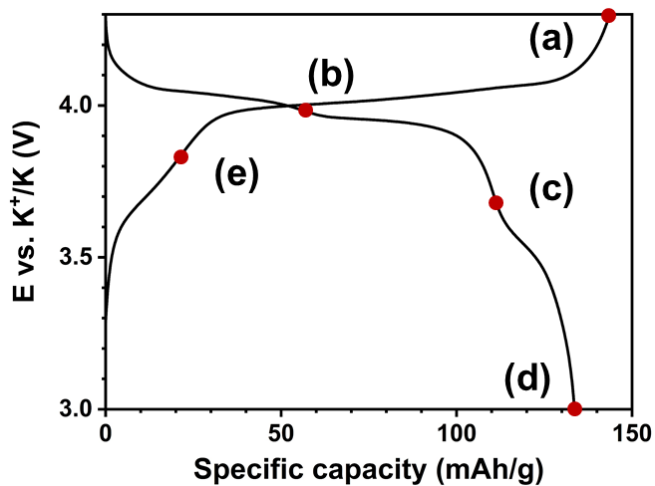| Δ (mm s^{-1})	δ (mm s^{-1})	Γ (mm s^{-1})	Area (%)	Site
0.00	-0.10(0)	0.29(0)	71	LS Fe^{2+}
1.49(2)	1.01(1)	0.36(2)	17(1)	HS Fe^{2+}
0.64(6)	0.30(5)	0.41(8)	12(2)	HS Fe^{3+}

Figure S4. Galvanostatic curve of MF21 | K half-cell at the current density of 5 mA/g with 5 selected states (red dots) at which *ex situ* Mössbauer spectra were recorded.

Table S3. Refined Room-Temperature ^{57}Fe Mössbauer Hyperfine Parameters for MF21 at different potentials.

| Potential	Δ (mm/s)	δ (mm/s)	Γ (mm/s)	Area (%)	Site
4.3 V (EOC)	0.00	-0.09	0.4(1)	11	LS Fe^{2+}
	0.35(3)	0.35	0.58(5)	31(2)	HS Fe^{3+}
	0.75(2)	-0.17	0.49(2)	58(5)	LS Fe^{3+}
3.9 V (discharge)	0.00	-0.11(0.00)	0.43(1)	72	LS Fe^{2+}
	0.28(2)	0.36(1)	0.43(3)	28(1)	HS Fe^{3+}
3.65 V (discharge)	0.14(0)	-0.11(0)	0.27(0)	70	LS Fe^{2+}
	0.28(2)	0.46(1)	0.55(3)	30(1)	HS Fe^{3+}
3 V (EOD)	0.00	-0.09(0)	0.32(0)	68	LS Fe^{2+}
	1.50(4)	1.13(2)	0.40(4)	19(2)	HS Fe^{2+}
	0.69(7)	0.40(5)	0.46(8)	13(3)	HS Fe^{3+}
3.8 V (charge)	0.12(0)	-0.10(0)	0.25(1)	72	LS Fe^{2+}
	0.26(5)	0.43(2)	0.59(8)	28(2)	HS Fe^{3+}
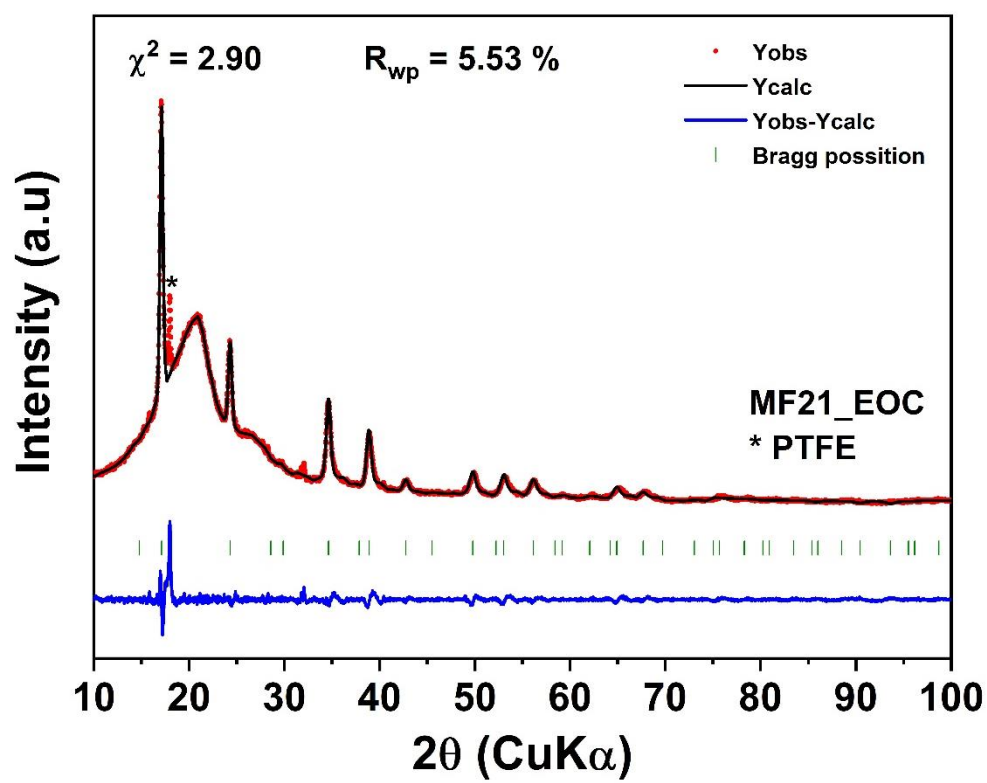
Figure S5. *Ex situ* XRD with Le Bail refinement of MF21 at the end of charge.
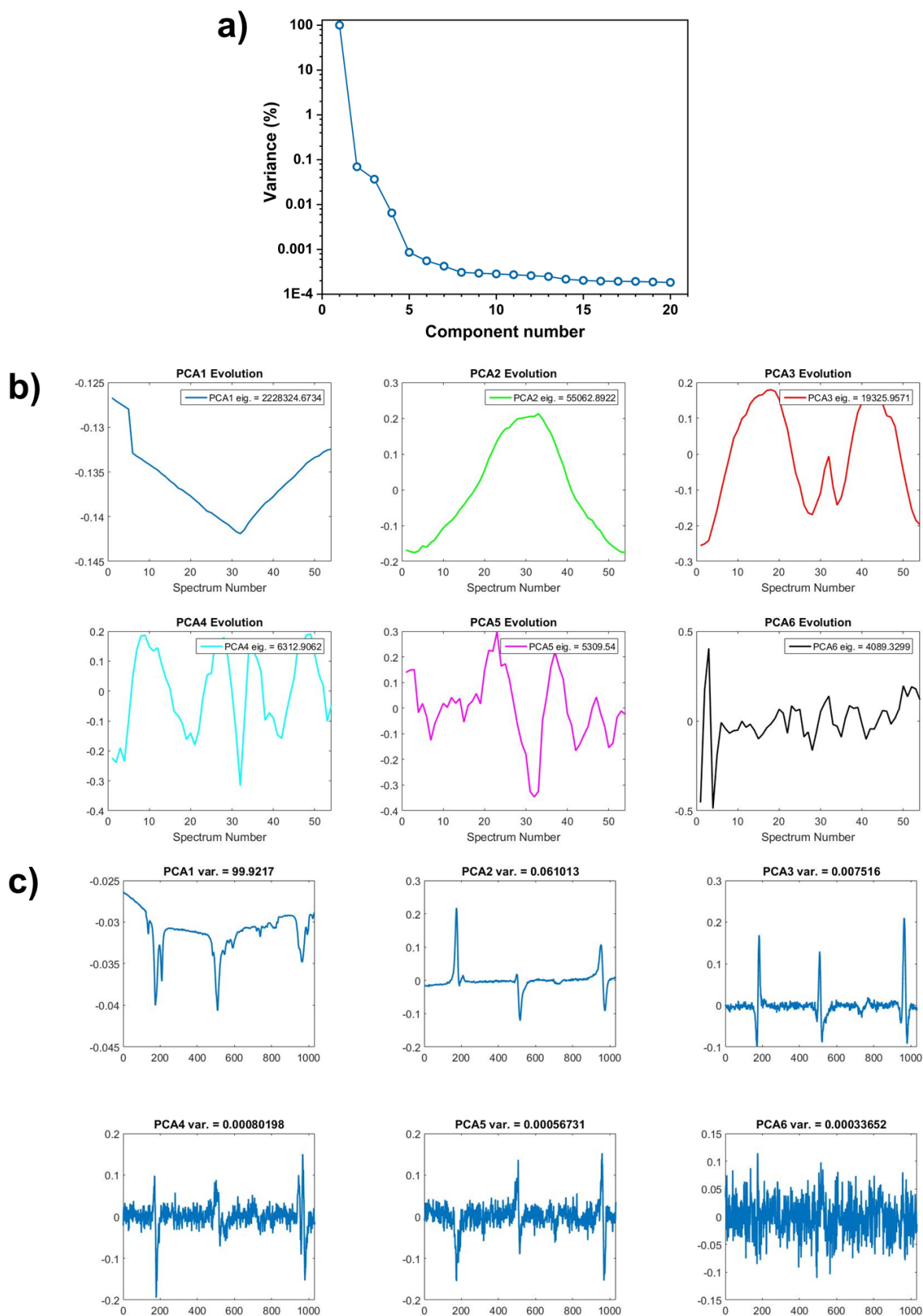
Figure S6. (a) Variance plot, (b) the evolution and (c) the patterns of principle components of the *operando* XRD dataset in the first K$^+$ extraction-insertion cycle of MF21.
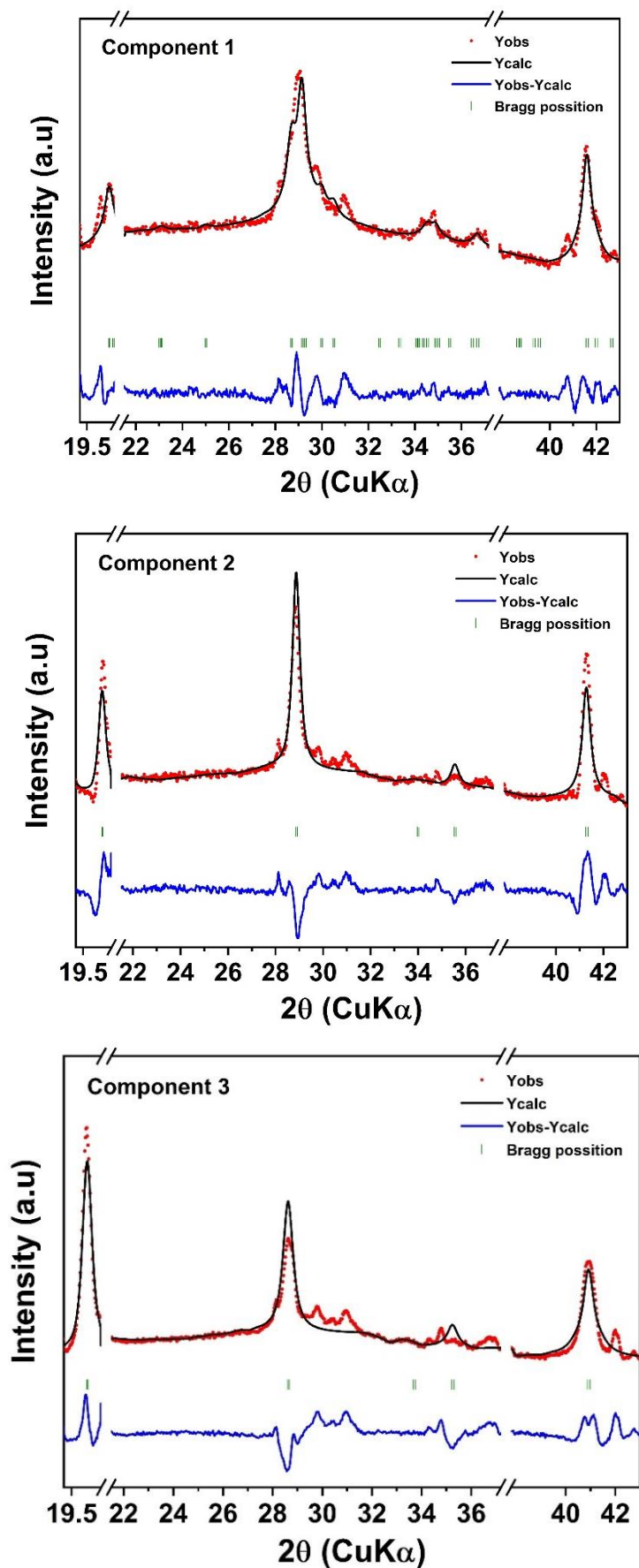
Figure S7. Profile matching refinement of three principal components of *operando* XRD dataset. The unfitted contributions in the region 30°-32° are a background signal originating from other compounds contained in the operando cell, such as PTFE, carbon black, Be window, Al foil and corresponding oxidation species. Also the precipitation of some electrolyte salt might contribute to this background signal.

Table S4. Lattice parameters of three MCR-ALS pure components obtained from Le Bail refinement.

Component	SG	a (Å)	b (Å)	c (Å)	β (°)	V/Z (Å³)
1	$P2_1/n$	10.087(1)	7.184(2)	6.967(6)	90.40(7)	252.4
	(*)	10.007	10.007	10.087	90	252.5
2	$Fm\bar{3}m$	10.159(1)	10.159(1)	10.159(1)	90	262.1
3	$Fm\bar{3}m$	10.244(1)	10.244(1)	10.244(1)	90	268.8

(*) Normalized parameters in a pseudo-cubic lattice based on the calculation in Ref. [2]

Figure S8. (a) Variance plot, (b) the evolution and (c) the patterns of principle components of the *operando* XAS dataset at Fe K edge in the first K⁺ depotassiation of MF21.
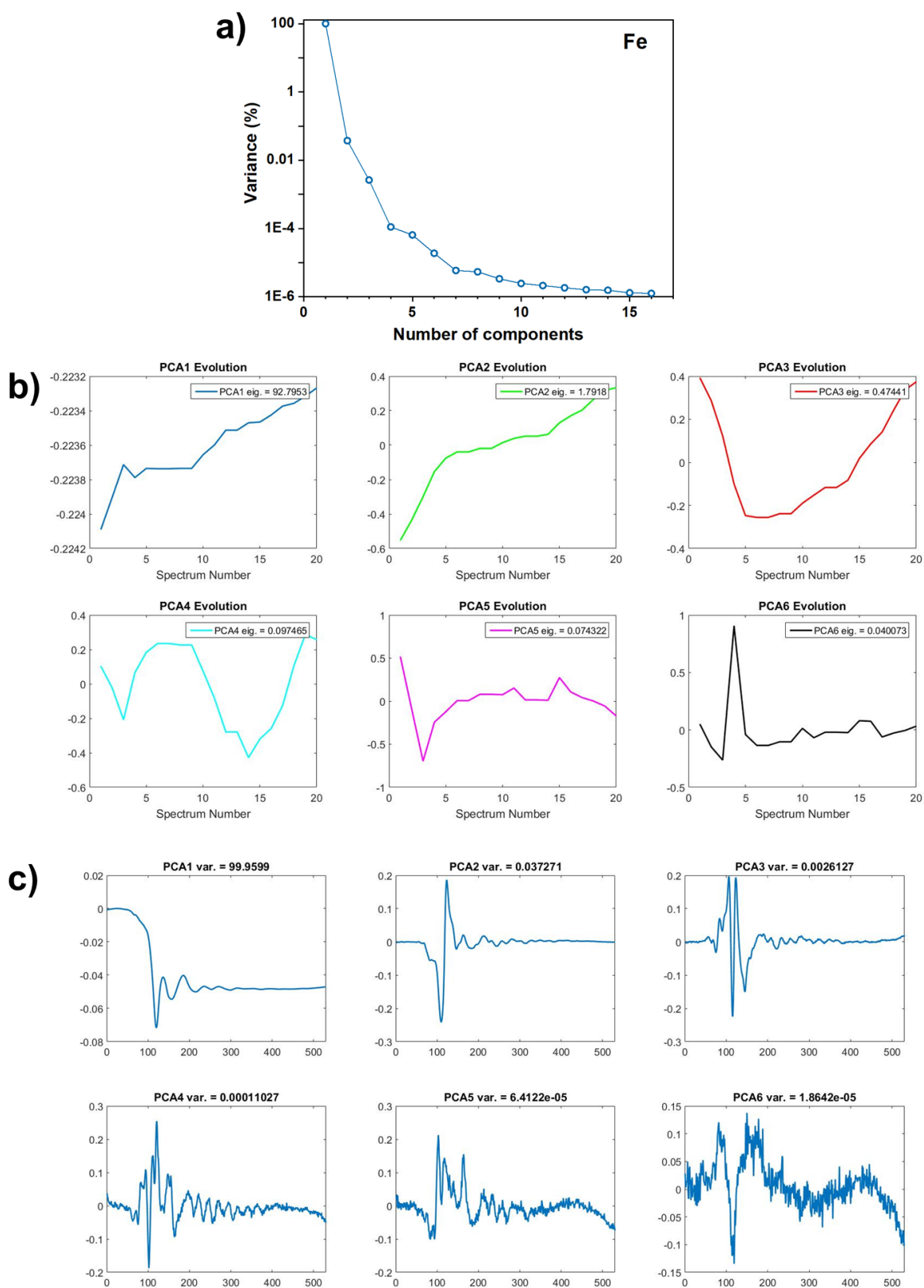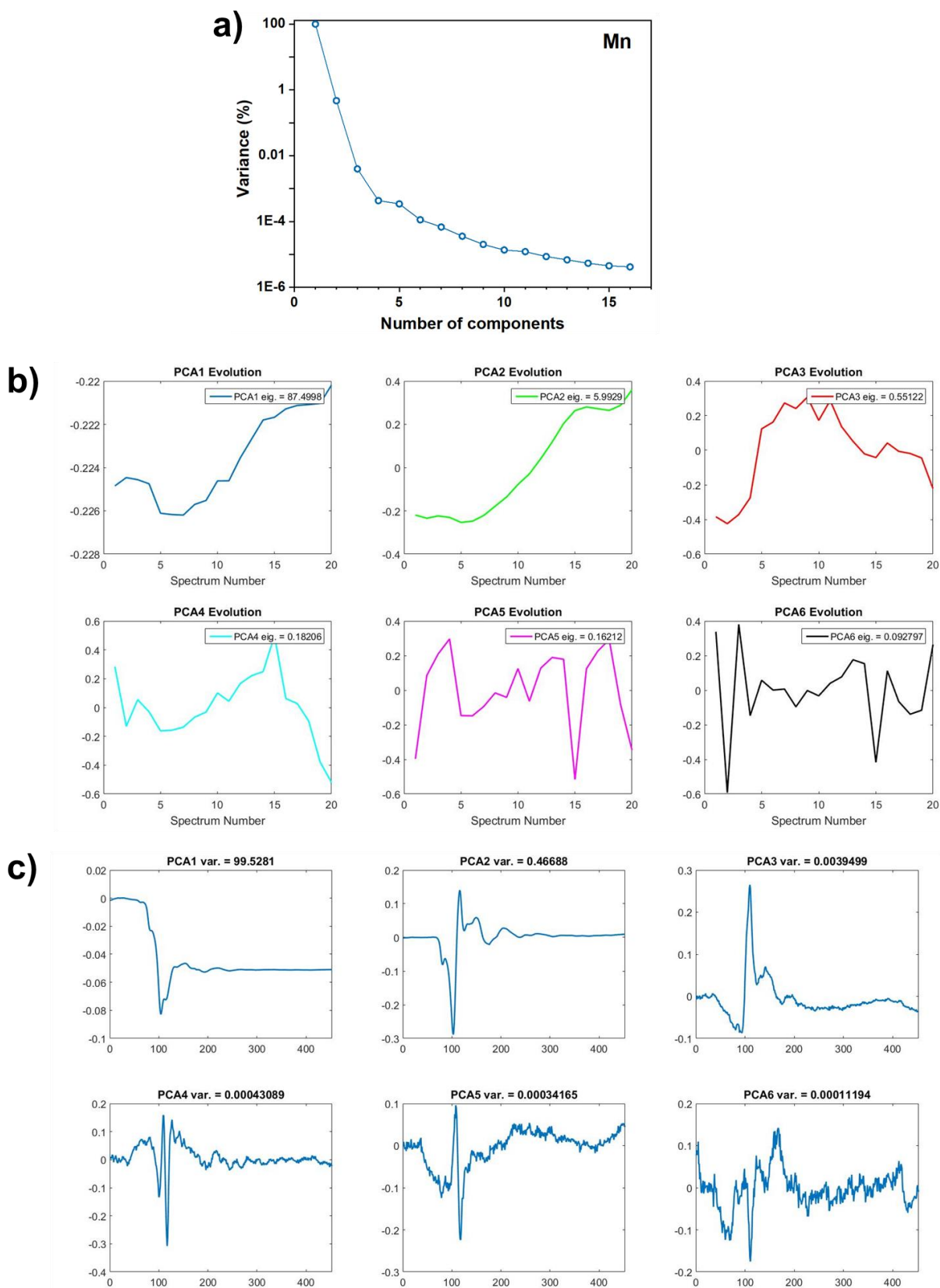
Figure S9. (a) Variance plot, (b) the evolution and (c) the patterns of principle components of the *operando* XAS dataset at Mn K edge in the first K⁺ depotassiation of MF21.
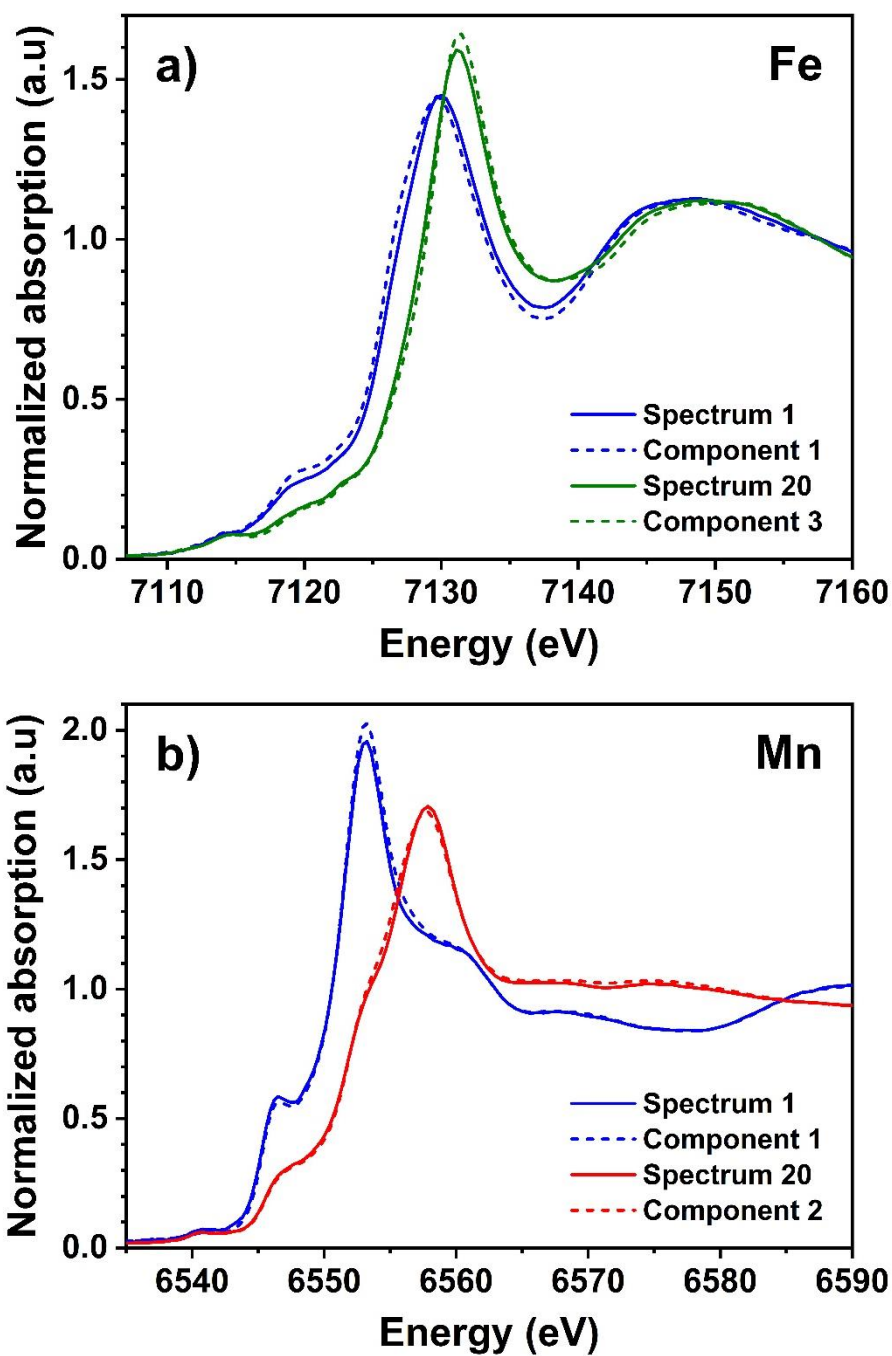
Figure S10. Comparison of the XANES part of Fe (a) and Mn (b) K edge of experimental spectra (solid lines) corresponding to the pristine and fully depotassiated phases with the first and last pure components (dash lines) constructed from MCR-ALS analysis.

Table S5. Parameters resulting from the fit of the pure components related to the Fe K edge spectra of MF21 during the depotassiation. The coordination numbers were multiplied with the percentage of each correspondent metal sites, which were inferred starting from the iron speciation obtained by Mössbauer spectroscopy.

Component	Shell	N	R_{theo} (Å)	R_{fit} (Å)	σ^2
1	Fe-C	4.32	1.84	1.88(1)	0.006(1)
	Fe-N	1.68	2.25	2.21(1)	0.005(2)
	Fe-C≡N	8.64	2.97	3.07(2)	0.006(1)
	Fe-N≡C	3.36	3.21	3.12(6)	0.005(2)
	Fe-C≡N-M	6	5.01	4.96(2)	0.011(3)
	Fe-K (*)	4.9	4.33	4.37(3)	0.015(5)
	Fe-K (**)	1.9	4.58	4.55(4)	0.004(5)
2	Fe-C	4.32	1.93	1.88(1)	0.004(1)
	Fe-N	1.68	1.93	2.03(2)	0.004(1)
	Fe-C≡N	8.64	3.15	3.08(1)	0.004(1)
	Fe-N≡C	3.36	3.15	3.22(1)	0.004(1)
	Fe-C≡N-Fe	6.4	5.08	5.15(3)	0.005(4)
	Fe-C≡N-Mn	5.6	5.08	5.31(6)	0.005(4)
	Fe-K	2	4.33	4.50(5)	0.013(8)
	Fe-C≡N-M-N (***)	13.4	5.53	5.5(2)	0.005(4)
	Fe-N≡C-Fe-C (***)	34.6	5.53	5.39(3)	0.005(4)
3	Fe-C	4.32	1.95	1.93(1)	0.003(1)
	Fe-N	1.68	1.95	2.06(2)	0.003(1)
	Fe-C≡N	4.32	3.18	3.11(1)	0.004(1)
	Fe-N≡C	1.68	3.18	3.25(1)	0.004(1)
	Fe-C≡N-Fe	6.38	5.19	5.21(3)	0.006(1)
	Fe-C≡N-Mn (s)	3.75	5.12	4.81(2)	0.006(1)
	Fe-C≡N-Mn (l)	1.87	5.12	5.4(1)	0.006(1)

(*) single scattering from LS Fe to K$^+$ neighbors

(**) single scattering from HS Fe to K$^+$ neighbors

(***) obtuse triangle

(s): short Mn–N bonding

(l): long Mn–N bonding

Table S6. Parameters resulting from the fit of the pure components related to the Mn K edge spectra of MF21 during the depotassiation.

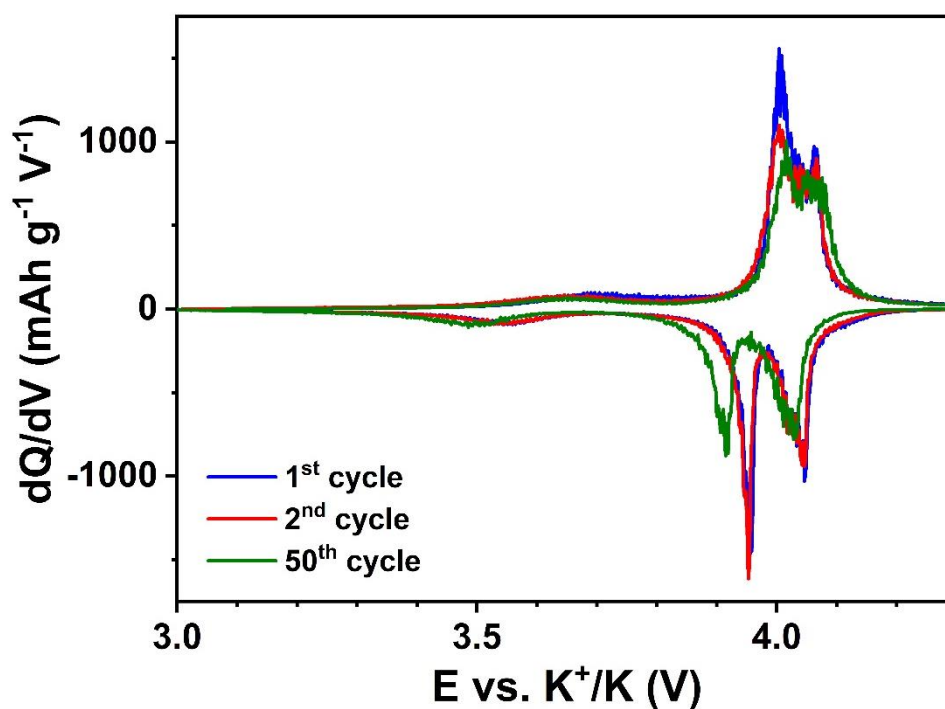| Component	Shell	N	R_{theo} (Å)	R_{fit} (Å)	σ^2
1	Mn-N	6	2.12	2.24(1)	0.008(1)
	Mn-N≡C	6	3.18	3.42(2)	0.013(3)
	Mn-N≡C-Fe	6	5.01	5.11(3)	0.017(4)
	Mn-K	6.8	4.33	4.58(5)	0.029(1)
2	Mn-N (1)	4	1.95	1.93(1)	0.014(1)
	Mn-N (2)	2	1.95	2.42(3)	0.014(1)
	Mn-N≡C (1)	8	3.18	3.03(2)	0.012(1)
	Mn-N≡C (2)	4	3.18	3.54(3)	0.012(1)
	Mn-N≡C-Fe (1)	8	5.12	4.99(2)	0.015(2)
	Mn-N≡C-Fe (2)	4	5.12	5.31(5)	0.015(2)

Figure S11. Derivative capacity of MF21 after 1, 2, and 50 cycles constructed from galvanostatic profiles in Figure 2.

References

1 D. Parajuli, H. Tanaka, K. Sakurai, Y. Hakuta and T. Kawamoto, *Materials*, 2021, **14**, 1151.

2 X. Bie, K. Kubota, T. Hosaka, K. Chihara and S. Komaba, *Journal of Materials Chemistry A*, 2017, **5**, 4325–4330.